Ceramics International 44 (2018) 10806–10812

Contents lists available at ScienceDirect

Ceramics International

journal homepage: www.elsevier.com/locate/ceramint

Blocking effect in promising proton conductors based on $Ba_3Ca_{1.18}Nb_{1.82-x}R_xO_{9-\delta}$ ($R = Y^{3+}$, Gd^{3+}, Sm^{3+}, Nd^{3+}) ordered perovskites for PC-SOFCs

L.H. Francisco[a], J.E. Rodrigues[a,b,*], W.R. Correr[a], A.C. Hernandes[a]

[a] Crystal Growth and Ceramic Materials Research Group, São Carlos Institute of Physics, University of São Paulo, CEP 13560-970 São Carlos, SP, Brazil
[b] Optical Spectroscopy and Raman Scattering Research Group, Department of Physics, Federal University of São Carlos, CEP 13565-905 São Carlos, SP, Brazil

ARTICLE INFO

Keywords:
$Ba_3Ca_{1.18}Nb_{1.82}O_{9-\delta}$
Proton conductor
Brick-layer
Space-charge
Impedance spectroscopy

ABSTRACT

High proton conductivity and good chemical stability are keys to development of new electrolytes for PC-SOFCs as the next-future energy generation systems. However, the extensive use of new polycrystalline materials as solid electrolytes is still avoided, since the grain boundary response usually leads to a decrease in total conductivity due to electrical blocking effect. Here, we present our results on the space-charge modeling of impedance spectroscopy data obtained for $Ba_3Ca_{1.18}Nb_{1.82-x}R_xO_{9-\delta}$ proton conducting ceramics, where $x = 0$, 0.30 and $R = Y^{3+}$, Gd^{3+}, Sm^{3+}, Nd^{3+} are doping agents. Non-stoichiometric barium calcium niobate perovskites have received much attention as potential solid electrolytes for proton conducting solid oxide fuel cells. We show that despite their increased grain conductivity, the doped ceramics possess Schottky barriers that are higher than those observed for undoped $Ba_3Ca_{1.18}Nb_{1.82}O_{9-\delta}$. In view of the space-charge model, proton depletion at the space-charge layer is the reason for the reduction of grain boundary conductivity in the doped compositions. Our findings are important for the understanding of proton conduction mechanisms in polycrystalline materials, which may allow future optimization of new doped electrolytes based on barium calcium niobate perovskites.

1. Introduction

Obtaining and optimization of highly efficient materials for energy generation define the state-of-art of the current investigations in materials science and materials chemistry, which are focusing on reducing environmental pollution and prevent global warming [1]. In particular, proton conducting solid oxide fuel cells (PC-SOFCs) are good candidates for future power generation, because they usually lower the SOFCs operating temperatures to intermediate values of 500–700 °C [2,3]. For practical applications, the chemical and mechanical stabilities under CO_2 and humid atmospheres should be taken into account during the optimization of candidates as PC-SOFCs electrolytes [4]. It is important to emphasize that the high resistivity of grain boundaries (also known as blocking effect) in the electrolytes also prevents their commercialization for intermediate temperature applications, once this feature introduces a decrease in the total conductivity [5–7]. However, until now, few studies in the literature are focused on the origin of the blocking effect in new candidates for PC-SOFCs electrolytes, H_2 sensors, or steam electrolysers [8].

From the materials science point of view, most of the studies have been targeted the standard $BaCeO_3$-$BaZrO_3$ simple perovskites. While the cerium-based electrolytes have high proton conductivity, zirconates possess good chemical stability in CO_2-rich atmospheres. In the last decades, many studies have devoted their attention to optimize the properties of cerate-zirconates, in which rare-earth elements are considered as dopants to create oxygen vacancies in the crystal structure [9]. Otherwise, new compositions are taking place as novel proton conductor electrolytes with satisfactory chemical stability. Among all the reported new ceramic-based electrolytes, $Ba_3Ca_{1.18}Nb_{1.82}O_{9-\delta}$ (BCN-18) has demonstrated reasonable results concerning both proton conductivity and chemical stability under extreme ambient conditions, making it feasible as electrolyte membrane for PC-SOFCs [10,11].

We should mention the results obtained by Wang et al. on the Y-doped BCN-18, showing that the composition $Ba_3Ca_{1.18}Nb_{1.52}Y_{0.30}O_{9-\delta}$ has an improved proton conductivity of about 5.3×10^{-3} Scm^{-1} at 600 °C in comparison with pristine one, besides its salable stability toward carbon dioxide and water (> 24 h resistant at 700 °C) [12]. Zhu et al. doped BCN-18 with Ni^{2+} (Ni into Nb sites) in order to improve its sinterability and elevate the proton conductivity, reaching values of 4.6×10^{-3} Scm^{-1} at 700 °C [13]. Unlike the simple perovskite with disorder at B-site, BCN-18 is described by an ordered superlattice with the 1:1 stacking sequence of −(Ca,Nb)−Nb−(Ca,Nb)−Nb− along

* Corresponding author at: Crystal Growth and Ceramic Materials Research Group, São Carlos Institute of Physics, University of São Paulo, CEP 13560-970 São Carlos, SP, Brazil.
E-mail addresses: lucash.francisco@gmail.com (L.H. Francisco), rodrigues.joaoelias@ifsc.usp.br, rodrigues.joaoelias@gmail.com (J.E. Rodrigues).
URL: http://www.ifsc.usp.br (L.H. Francisco).

https://doi.org/10.1016/j.ceramint.2018.03.121
Received 10 January 2018; Received in revised form 10 March 2018; Accepted 13 March 2018
Available online 14 March 2018
0272-8842/ © 2018 Elsevier Ltd and Techna Group S.r.l. All rights reserved.

the $[111]_c$ planes of the B-site ordered cubic cell. The non-stoichiometric Ca^{2+} not only leads to oxygen vacancies, but also allows a modification in the cationic order-type that improves the proton conductivity coming from the ceramic grains [14].

In this paper, we explore the intrinsic origin of the blocking effect in a novel candidate for PC-SOFCs in light of the space-charge model, allowing us to develop a basic understanding of the intrinsic electric response coming from the grain boundaries in proton conducting ceramics based on ordered perovskites. For this purpose, we synthesized new ceramic materials $Ba_3Ca_{1.18}Nb_{1.82-x}R_xO_{9-\delta}$, such that $x = 0$, 0.30 and $R = Y^{3+}$, Gd^{3+}, Sm^{3+}, Nd^{3+}. The variation of rare earth elements aims the evaluation of both radius and polarizability effects of the doping elements on the electrical properties. We also combined the impedance spectroscopy technique and the brick-layer model to correctly assign the electrical response coming from the grains and grain boundaries. The structural and morphological properties of the ceramic samples were investigated using powder X-ray diffraction, Raman spectroscopy and scanning electron microscopy.

2. Theoretical analyses

2.1. Brick-layer model

The brick-layer model (BLM) takes grains and grain boundaries as two distinct phases distributed through the material as a network of identical cubes (grains), being separated by boundary phase layers [15,16], as shown in Fig. 1**(a)**. Assuming that electrical current flows only at applied electric field direction, there are two possible conduction branches: (#1) a sequence of long narrow boundaries (parallel grain boundaries) and (#2) a sequence of intercalating grain cubes and thin boundary layers (perpendicular grain boundaries), see in Fig. 1**(b)**. A general model for the material must consider these two paths as parallel circuit branches. Fig. 1**(c)** displays such a circuit, where each individual phase is modelled by a parallel unit containing R||CPE||C elements. A capacitor is added to the conventional R||CPE unit for modeling the high frequency limiting capacitance value, as recently suggested by Hernández et al. [17]. In most cases, due to unfavorable geometry of parallel grain boundaries (gb||) in addition to usual greater boundary phase resistivity, the grain-perpendicular boundary ($gb_\perp$) branch is the favorable conduction path and the parallel boundary circuit section is usually excluded from the model [18]. Details on BLM can be found in Table S1 of Supplementary information.

2.2. Space-charge model

The intrinsic grain boundary conductivity in proton conductors is successfully interpreted in terms of the space-charge model (SCM) [19,20], in which grain boundaries are represented as a positively charged core surrounded by a negatively charged depletion region. The concentration of acceptor dopant is considered constant everywhere outside boundary core (i.e. Mott-Schottky approximation), so that the negative layer arises only from depletion of positive $OH^{\bullet}$ defects. The potential barrier $[\Delta\varphi(0) = \varphi(0) - \varphi(\infty)]$ is the intrinsic potential barrier (i.e. Schottky barrier) imposed to the defect transport through grain boundaries. The direct evidence for the presence of such potential barriers on proton conductors has been provided by biased voltage impedance spectroscopy investigations [21,22]. Considering the charge density at the depletion region as being uniform and equal to acceptor dopant volumetric charge density, the equations relating the model parameters to experimentally accessible electrical quantities can be derived [19]. The potential barrier height is directly related to the intrinsic grain and grain boundary conductivities obtained from the brick-layer model by the equation:

$$\frac{\sigma_g}{\sigma_{gb\perp}} = \frac{k_B T}{2e\Delta\varphi(0)} \exp\left[\frac{e\Delta\varphi(0)}{k_B T}\right], \tag{1}$$

where σ_g and $\sigma_{gb\perp}$ are the grain and grain boundary conductivities; $\Delta\varphi$ denotes the potential barrier; e, k_B and T maintain their usual meaning. Here, we denote charge density of dopant atoms by $\rho_{Q:\,R}$, being calculated based on the nominal chemical composition of the material. We may define the space-charge layer width λ^* related to the Debye length L_D, as follows:

$$\lambda^* = 2L_D\left(\frac{e\Delta\varphi(0)}{k_B T}\right)^{\frac{1}{2}}, \ \textit{where}\ L_D = \left(\frac{\varepsilon \cdot k_B T}{2e\cdot\rho_{Q:R}}\right)^{\frac{1}{2}}, \tag{2}$$

such that ε is the dielectric constant. The defect concentration profile $c_{OH^{\bullet}}(r)$ normalized with respect to the defect concentration at the grain's bulk $c_{OH^{\bullet}}(\infty)$ is given by the next expression:

$$\frac{c_{OH^{\bullet}}(r)}{c_{OH^{\bullet}}(\infty)} = \exp\left[-\frac{1}{4}\left(\frac{r-\lambda^*}{L_D}\right)^2\right]. \tag{3}$$

3. Experimental section

3.1. Powder synthesis

Powders of $Ba_3Ca_{1.18}Nb_{1.82-x}R_xO_{9-\delta}$ ($x = 0$, 0.30 and $R = Y^{3+}$, Gd^{3+}, Sm^{3+}, Nd^{3+}), hereafter BCN-*R* system, were synthetized by a conventional solid state reaction. Starting powders of $BaCO_3$ (Alfa Aesar; 99.80%), $CaCO_3$ (Alfa Aesar; 99.95%), Nb_2O_5 (CBMM-Araxá, Brazil; optical degree), Y_2O_3 (Alfa Aesar; 99.9%), Sm_2O_3 (Alfa Aesar; 99.9%), Nd_2O_5 (Fluka; 99.9%) and Gd_2O_3 (Alfa Aesar; 99.99%) were stoichiometrically weighted and mixed for 24 h by milling in isopropyl alcohol with zirconia cylinders. The dry mixtures were calcined in air at 1473 K for 5 h and milled in a 4:5 mass fraction solution of isopropyl alcohol in relation to the powder mass. The last calcination and milling steps were repeated to ensure homogeneous phase attainment.

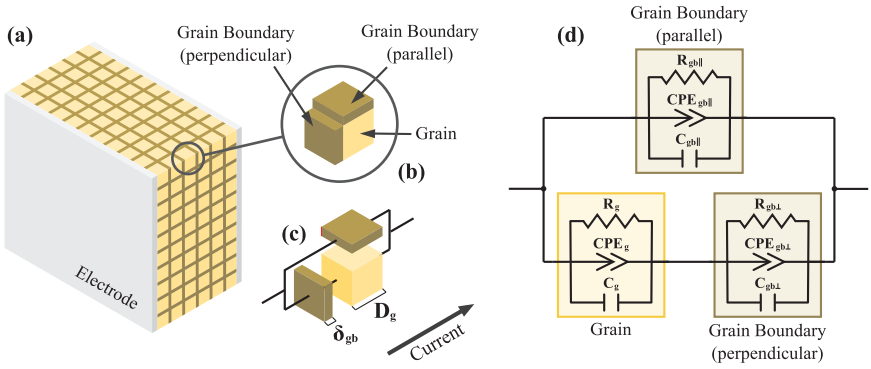

Fig. 1. (a) Ceramic material with metallic electrodes on two opposite flat faces. Microstructure is represented as a lattice of cubic grains intercalated with thin grain boundaries, as described by the brick-layer model. (b) The ceramic microstructure is composed of units containing one grain and two boundary units, one perpendicular and one parallel to current direction. (c) Circuit representation of the microstructure in (b) emphasizing the presence of two possible current paths. (d) Equivalent circuit model for the ceramic sample, where each homogeneous phase is represented as a parallel R||CPE||C unit.

3.2. Sintering

Samples of the final powders were pressed into disks (ϕ = 7 mm × H = 2 mm) by a uniaxial pressure of 15 MPa for 2 min followed by cold isostatic pressing at 300 MPa for 10 min. The pellets were then sintered at 1823 K for 12 h in air with heating and cooling rates of 2 K min^{-1} and 10 K min^{-1}, respectively.

3.3. (Micro)structural characterization

Structural characterization of the ceramic samples was made using powder X-ray diffraction (PXRD) on a Rigaku Ultima IV X-ray diffractometer with Cu-Kα radiation (λ = 1.54056 Å; 40 kV and 30 mA). Diffraction patterns were collected on ranges 10°-100° (1° min^{-1}, continuous mode), 29.0-30.8° and 17.4-18.9° (0.015° step scan mode; 20 s per step). Raman spectra were recorded at room temperature without heat pretreatments by a HR800 Evolution micro-Raman spectrometer (Horiba *Jobin-Yvon*) in a backscattering geometry with 1800 gr mm^{-1} holographic grating (resolution ~ 1 cm^{-1}). The Nd:YAG 532 nm laser line was employed as an excitation source, being focused on the sample surface by a 50 × objective (NA = 0.35). For microstructure observation, polished samples were analyzed by an Inspect F-50 scanning electron microscope (SEM) equipped with an energy dispersive X-ray spectrometer (EDXS). Details on the compositional studies can be found in Table S2 of Supplementary information. For bulk density determination, two procedures were employed, namely immersion method and geometric one. In the first case, the Archimedes principle was taken into account using distilled water as an immersion liquid. In the last case, the size dimensions and mass of the sintered ceramics were considered as inputs.

3.4. Electrical characterization

Electrical properties were measured by means of impedance spectroscopy (IS) technique using a Solartron 1260 Impedance Analyzer with Solartron 1296 A Dielectric Interface. Prior to the impedance experiments, the ceramic samples with sputtered platinum electrodes were maintained at 823 K for 12 h in a homemade furnace, being held using a weak mechanical pressure. The electrical impedance measurements were made on such ceramics in air from 440 K down to room temperature during a controlled cooling with rate of 1 K min^{-1}. The complex impedance spectra [$\mathbf{Z} = \mathrm{Re}(\mathbf{Z}) + j\mathrm{Im}(\mathbf{Z})$] in the frequency range between 100 mHz and 1 MHz were obtained under temperature plateaus with dwell time of about 1 h to guarantee an isothermal condition at the sweep frequency with 20 points per decade. Heating/cooling cycles were performed in our ceramics, showing a good reproducibility. The ZView software 2.9c was employed to analyze and adjust the spectral data [23].

4. Results and discussion

4.1. Structural disorder and microstructure

Fig. 2**(a)** shows the powder X-ray diffraction patterns for ceramic samples of all the compositions indexed with respect to a double perovskite $Ba_2Ca_{1+y}Nb_{2-y}O_6$ structure that belongs to the *Fm*-3*m* (O_h^5 or #225) space group [14]. No minor secondary phases were detected in the diffraction patterns. Reflections (111) and (220) measured in step-scan mode are exhibited in Fig. 2**(b-c)**, being fitted using the pseudo-Voigt profiles. As chemical composition is modified, no phase alteration was observed aside from peak shift related to the lattice constant changes. Fig. 2**(d)** displays the lattice constants calculated from the measured patterns, corroborating the *d*-spacing shift behavior as a consequence of the unit cell increase. The presence of (111) peaks in all the diffraction patterns is a signature of 1:1 B-site ordering at [111] direction. Fig. 2**(e)** illustrates the 1:1 ordering pattern where two non-equivalent octahedra are packed in a cubic NaCl-like ordered lattice (or rock-salt).

Structure factor calculations for this ordered structure show that only when the octahedra are identical the (111) intensity must vanish, according to the following equation:

$$F_{111} = 4(f_{B'} - f_{B''}) + 24f_O \sin(2\pi\Delta a), \quad (4)$$

where $f_{B'}$, $f_{B''}$ and f_O are the atomic form factors of B', B'' and oxygen ions and Δa is the difference in size between the non-equivalent octahedra $B'O_6$ and $B''O_6$. Since it was detected the (111) reflection in all the diffraction patterns, we can further conclude that all the BCN-*R* ceramics possess an octahedral 1:1 long-range ordering at B-site, as sketched in Fig. 2**(e)**. We can also estimate the degree of order using the ratio Ψ, being defined as the ratio between (111) and (220) peak intensities, as shown in Fig. 2**(d)**. One should note a reduction in Ψ values after the incorporation of ~ 30% doping ions, denoting a decrease in the degree of 1:1 order at long-range in BCN-*R* ceramics.

For the 1:1 ordered cubic cell, four [$2\mathbf{F}_{2g} \oplus \mathbf{E}_g \oplus \mathbf{A}_{1g}$] Raman-active modes and four [$4\mathbf{F}_{1u}$] infrared ones are expected to appear in its first-order vibrational spectra [24]. Fig. 3**(a)** displays the Raman spectra at room temperature for the BCN-*R* ceramics, collected at their polished and cleaned surfaces. One should note Raman bands at 85–100, 300–375, 500–600 and 700–900 cm^{-1}, being attributed to the $\mathbf{F}_{2g}$, $\mathbf{F}_{2g}$, $\mathbf{E}_g$ and $\mathbf{A}_{1g}$ symmetry species [24], respectively. In Fig. 3**(b)**, a spectral decomposition by Lorentzian profiles in the interval 700–900 cm^{-1} was performed to better characterize its splitting process. It is possible to

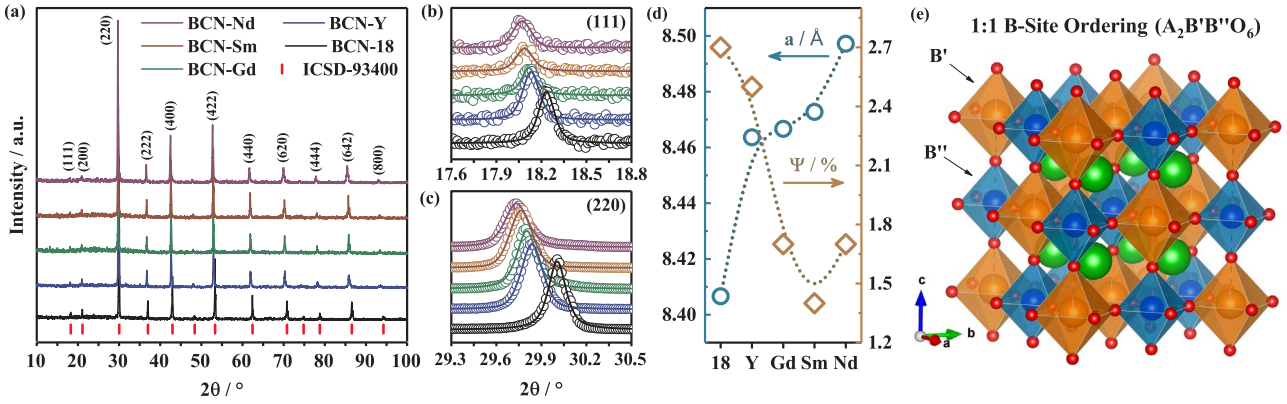

Fig. 2. (a) Powder X-ray diffraction patterns for BCN-*R* ceramics indexed with respect to an ordered double perovskite cubic structure (ICSD#93400). (b-c) Step-scan diffraction data for 2θ regions containing (111) and (220) peaks. (d) Lattice constants calculated from the diffraction patterns and the ratio Ψ = (111)/(220). Horizontal axis shows compositions in increasing order of B-site dopant radius. (e) Cristal structure of a double perovskite cubic structure displaying the B-site plane ordering at [111] direction, where B' = (Ca, Nb) and B'' = Nb. Structural figure was represented with the *VESTA* software.

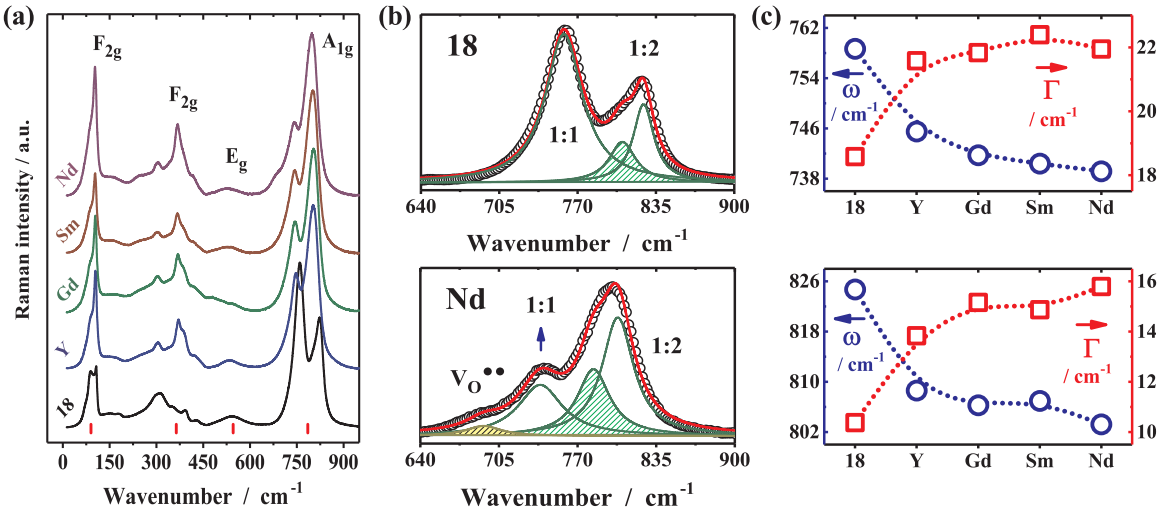

Fig. 3. (a) Raman spectra recorded at room temperature for the BCN-*R* ceramics. (b) Spectral decomposition process using Lorentzian profiles, where the black open circles denote experimental data and red solid lines are the fitted spectra. (c) Peak parameter data (ω-position and Γ-linewidth in units of cm^{-1}) as a function of the composition.

identify at least three modes in the wavenumber range between 640 and 900 cm^{-1}. In the Nd-doped ceramic a fourth band appeared at ~ 692 cm^{-1}. According to Valdez-Ramírez et al. [25], such a band is related to the oxygen vacancies and its intensity may indicate a total or partial filling of these vacancies by OH species. In this way, we concluded that oxygen vacancies in the BCN-Nd ceramic are partially filled by hydroxyl groups and full-filled in the remaining ceramics. This result also means that the protonic defects were created from the dissociative adsorption of water, as described by the next reaction:

$$H_2O_{(g)} + V_O^{\bullet\bullet} + O_O^{\times} \leftrightarrow 2OH_O^{\bullet}. \quad (5)$$

We should also mention the modes centered at 740–760 and 800–825 cm^{-1} whose peak parameters (ω-position and Γ-linewidth in units of cm^{-1}) are plotted as a function of the composition in Fig. 3**(c)**. Such modes are very sensitive to the disorder features at short-range in complex perovskites [26,27]. As a general behavior, the introduction of doping agents leads to peak broadening followed by a redshift in the peak position. The broadening process can be associated to the disorder effects, corroborating our earlier analysis using the ratio Ψ. In view of the spatial-correlation model [28], the reduction of the phonon correlation length leads to an increase in the linewidth. Besides, the redshift effect of the $\mathbf{A}_{1g}$ modes was directly attributed to the unit cell expansion due to the incorporation of doping ions. The combination of PXRD and Raman spectroscopy data allows us to conclude that the introduction of doping ions leads to a more disordered 1:1 structure for $Ba_3Ca_{1.18}Nb_{1.52}R_{0.30}O_{9-\delta}$ ceramics.

The microstructure of the BCN-*R* ceramics was investigated using scanning electron microscopy in order to evaluate the grain size distribution and possible phase segregation to the grain boundaries. Fig. 4 displays representative micrographs of all BCN-*R* ceramics thermal etched surfaces. It is clear the occurrence of small particles with D_g ~ 0.8 μm at the grain boundaries. An energy dispersive X-ray analysis revealed that such particles have the same nominal composition of BCN-*R* systems, as listed in Table S2. Besides, pore formation is observed and the grains have almost a honeycomb-like shape. It should be pointed out that such porosity may be originated during the polishing procedure prior the thermal etching, preventing any conclusion on porosity degree based on the micrographs of Fig. 4. In Supplementary information, Fig. S1 exhibits a boxplot with the size distribution of the BCN-*R* grains. The average grain size grew from 3–6 μm. However, in all cases, it can be clearly noticed a broad size distribution with standard deviation ranging from ~ 2 μm for BCN-18 to ~ 4 μm for BCN-Nd. Table 1 summarizes all data concerning the microstructural properties.

4.2. Electrical properties

In this study, the brick-layer model has been successfully applied to describe the electrical response of the BCN-*R* ceramics. A piece of evidence for this fact can be observed in Fig. 5, where it is exhibited the experimental and fitted Cole-Cole plots for BCN-*R* samples, respectively. One can note two well-resolved semicircle and a third contribution ascribed to the electrode polarization. Electrode contributions at low frequency were detected in most of the impedance spectra obtained here, which were modelled by a single CPE or a parallel R||CPE unit. Those semicircles are concerned to the grain and grain boundary in accordance with the BLM. Since we have used a condition where $R_{gb||} > > R_{gb\perp}$, one should not expect a current flow through the parallel grain boundary (branch #1) and then only two R||CPE||C units were used to adjust our impedance data (branch #2). From this circuit, we have extracted a set of values related to the resistance, capacitance and constant phase element (CPE) of the grain (R_g and C_g) and grain boundary ($R_{gb\perp}$ and $C_{gb\perp}$) for selected temperatures between 318 and 440 K.

As earlier reported, the incorporation of Ca^{2+} off-stoichiometry leads to both oxygen vacancy creation and B-site ordering transition from 1:2 to 1:1 [14]. In a recent work, our group has reported the isolated effects of B-site ordering on the conductivity properties of stoichiometric $Ba_3CaNb_2O_9$, concluding that 1:1 order elevates the total conductivity in comparison to the 1:2 order [24]. Indeed, the oxygen migration path through the NbO_6 octahedral units is energetically more favorable than along the edges of CaO_6 units [29]. Besides, experimental and theoretical results elucidated that the oxygen migration is ruled by the percolation path along NbO_6 octahedral network in the 1:1 cubic $Ba_3Ca_{1+z}Nb_{2-z}O_{9-\delta}$ ceramics. Regarding the electrical conductivity, we have focused here in understanding its intrinsic origin by separating the response coming from both grain and grain boundary.

The transport mechanism of the charge carriers was studied under both composition and temperature variation in dry condition. Table 1 shows the composition dependence of the grain conductivity (σ_g) for the BCN-*R* ceramics. As one can read, the conductivity attributed to the grains increased in doped samples. Such a result is a consequence of more oxygen vacancies being generated after the introduction of ~ 30% doping ions into the crystal structure, as described by Wang et al. [12]. In particular, the BCN-Gd depicted the higher value for the grain conductivity at 410 K. In Fig. 5**(b-f)**, one should note a thermal dependence of the resistivity spectra, describing a thermal activated process. Fig. 6**(a)** displays the Arrhenius-like plot for both grain (σ_g) and grain boundary ($\sigma_{gb\perp}$) conductivities for all the ceramic samples extracted

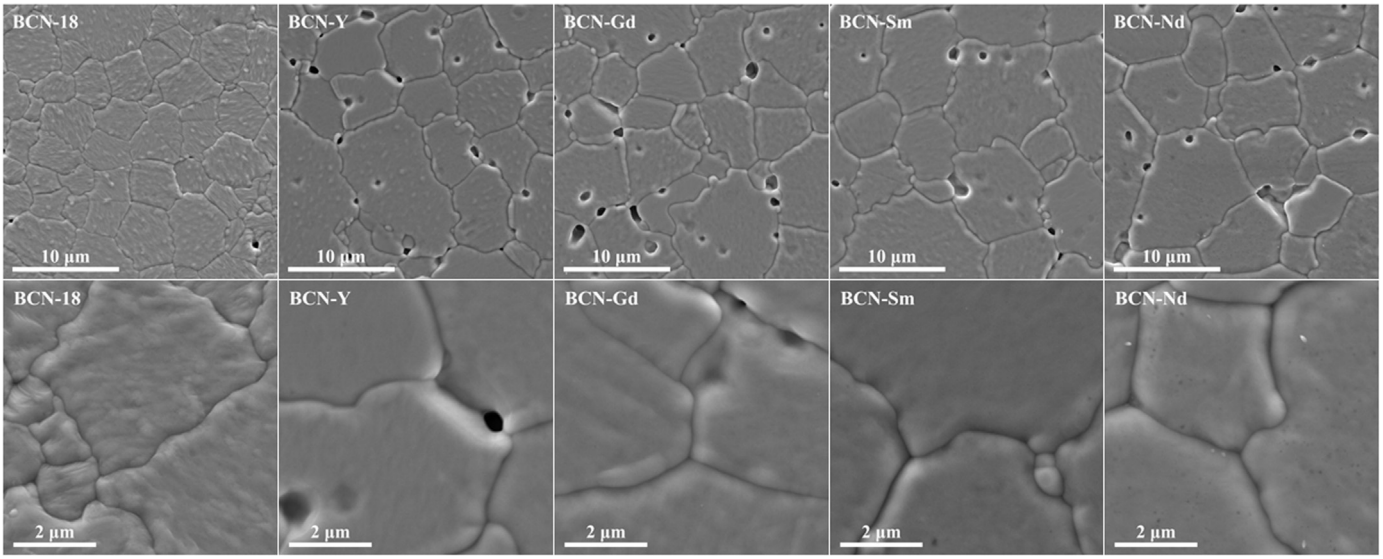

Fig. 4. (top-row) Scanning electron micrographs of the BCN-*R* ceramic surfaces after thermal etching. (bottom-row) Details of the grain and grain boundaries in order to better characterize possible phase segregation or liquid phases. All micrographs were obtained using back-scattered (BSE) mode.

from BLM. Using this plot, one can obtain the macroscopic activation energies attributed to the conductivity process.

Fig. 6**(b)** shows the activation energies associated to the conductivity processes coming from the grain and grain boundary. The energies for the grain conductivity range from ~ 0.60 and 0.70 eV, being ascribed to proton conduction in light of the Eq. (5). Even though activation energies for grains are higher for doped samples, they are the ones with higher values of bulk conductivity (see in Table 1), being caused by the greater charge carrier density introduced by doping. For the grain boundary conductivity, the transport mechanism has activation energies between 0.65 and 0.90 eV, denoting a blocking action by this microstructural region. Such values are slightly higher than those reported by Wang et al. [12] for measurements performed in wet air (3 vol% H_2O) for $Ba_3Ca_{1.18}Nb_{1.82-x}Y_xO_{9-\delta}$ system. At the grain boundary, it is also possible the contribution coming from electronic hole (p-type) to the electrical conductivity.

At the same time, the blocking factor (α_R) has increased in the BCN-*R* ceramics. Such a factor gives us a qualitative view on the fraction of the electric carriers that are blocked at the grain boundary surfaces, being defined as follows:

$$\alpha_R = \frac{R_{gb\perp}}{R_{gb\perp} + R_g} \times 100. \quad (6)$$

It is important to point out that the blocking factor does not depend on geometrical dimensions and we can use it to compare different samples [30,31]. Table 1 presents the calculated blocking factors for samples of all the compounds at 320 K and 410 K. The temperature sensibility of these values is linked to the differences between grain and grain boundary activation energies. For materials in which grain boundary energies are greater than those for grain, the blocking factor increases for lower temperatures. In BCN-Nd, its grain boundary energy is lower than grain energy, and then the opposite effect is observed. In BCN-Gd, for which no variation on blocking was observed at the considered temperature range, the activation energies are the closest for grain and grain boundary. Such a consideration illustrates how the wide variation (~ 0.25 eV) observed in grain boundary energy modifies the temperature dependence of the blocking effect.

The first hypothesis to explain the blocking behavior concerns the segregation of an insulating phase at the grain boundaries. For example, in doped zirconia the siliceous phase usually acts increasing the grain boundary resistance, and then the blocking factor [32]. Here, from both SEM and EDXS techniques, it was not observed any signal of liquid or glassy phase formation as a consequence of a possible secondary phase in the precursor powder. Likewise, porosity effects could be considered to explain the blocking features; however, there is no experimental basis to support the last hypothesis, since we have obtained highly

Table 1
List of chemical formula, space group, lattice constant, theoretical and relative densities, average grain size, and electrical parameters extracted from the impedance spectroscopy data in light of the brick-layer and space-charge models.

Sample	BCN-18	BCN-Y	BCN-Gd	BCN-Sm	BCN-Nd
Chemical formula	$Ba_3Ca_{1.18}Nb_{1.82}O_{9-\delta}$	$Ba_3Ca_{1.18}Nb_{1.52}Y_{0.30}O_{9-\delta}$	$Ba_3Ca_{1.18}Nb_{1.52}Gd_{0.30}O_{9-\delta}$	$Ba_3Ca_{1.18}Nb_{1.52}Sm_{0.30}O_{9-\delta}$	$Ba_3Ca_{1.18}Nb_{1.52}Nd_{0.30}O_{9-\delta}$
Space group, Z	*Fm-3m* (#225), 4	*Fm-3m* (#225), 4	*Fm-3m* (#225), 4	*Fm-3m* (#225), 4	*Fm-3m* (#225), 4
Lattice constant, a_F (Å)	8.406(7)	8.463(1)	8.466(1)	8.479(1)	8.497(2)
Theoretical density (g cm^{-3})	5.76	5.63	5.78	5.74	5.69
Relative density, immer. | geom. (%)	- | 96 ± 1	- | 96 ± 1	98.3 ± 0.3 | 97 ± 1	98.2 ± 0.5 | 96 ± 1	97.9 ± 0.3 | 96 ± 1
Average grain size, D_g (µm)	3.2	4.3	4.6	4.2	6.7
Grain boundary thickness, δ_{gb} (nm)	3.0	1.9	2.6	1.6	3.6
Act. energy of grain (eV)	0.60	0.67	0.67	0.70	0.70
Act. energy of g. boundaries (eV)	0.78	0.90	0.71	0.77	0.65
Grain conductivity at 410 K, σ_g (S cm^{-1})	3.3×10^{-6}	6.8×10^{-6}	7.3×10^{-6}	6.7×10^{-6}	6.9×10^{-6}
Blocking parameter at 320 K, α_R (%)	68	96	96	95	86
Blocking parameter at 410 K, α_R (%)	33	81	96	93	90
Schottky barrier at 320 K, $\Delta\phi(0)$ (V)	0.30	0.39	0.38	0.39	0.35
Schottky barrier at 410 K, $\Delta\phi(0)$ (V)	0.30	0.43	0.49	0.49	0.46
SCM layer width, $2\lambda^*$ (nm)	1.8	1.3	1.5	1.5	1.3

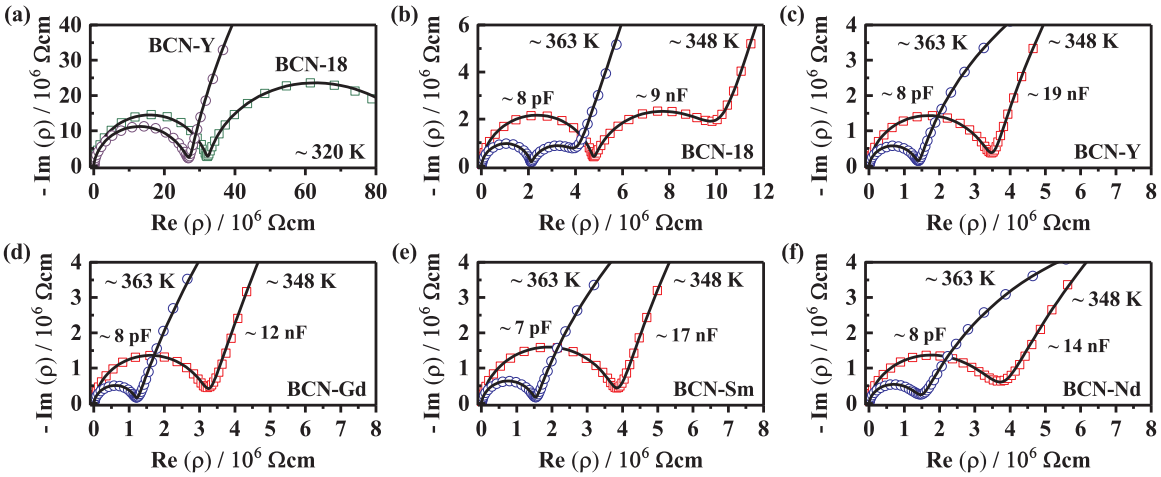

Fig. 5. Cole-Cole plots for impedance spectra of BCN-*R* ceramic samples, respectively. Solid lines represent equivalent circuit fitting for each spectrum.

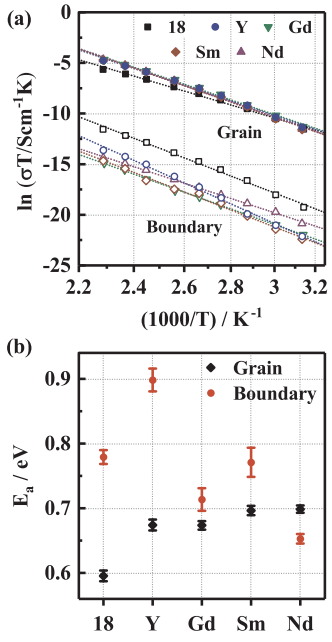

Fig. 6. (a) Reciprocal temperature dependences of both σ_g and $\sigma_{gb\perp}$ conductivities for BCN-*R* ceramics. (b) Activation energies for grain and grain boundary conductivities of all the ceramic compositions derived from the Arrhenius plots.

dense ceramics (> 96-98%) with porosity degree less than 4-2%, see in Table 1.

In such a way, the blocking phenomena in doped $Ba_3Ca_{1.18}Nb_{1.82}O_{9-\delta}$ ceramics should have an intrinsic origin attributed to the proton depletion in the space-charge layer, being it responsible for the reduction of the grain boundary conductivity. Based on this assumption, we have applied the space-charge model to better explain the blocking effect in BCN-*R* ceramics, starting from the potential barrier $\Delta\varphi(0)$ determination using Eq. (1) in the context of the Mott-Schottky approximation [33]. Table 1 shows the potential barrier (also known as Schottky barrier) values at 410 K. The barrier was increased after the incorporation of doped cations into the crystal structure of BCN-18.

A diagram containing details on the charge distribution in the surrounding of the grain boundary is shown in Fig. 7**(a)**. In such a representation, the grain boundary region is defined as a positive core followed by a negative charge zone. The depletion of the protonic defects $OH^{\bullet}$ is inversely related to the electrostatic potential $\varphi(r)$ between the grain interior and grain boundary core. As a consequence, the macroscopic conductivity coming from the grain boundary tends to decrease for an increased potential barrier, leading to the blocking effect detected in doped ceramics.

It is worth mentioning that the grain boundary thickness (δ_{gb}) is almost twice the space-charge layer width (λ^*). Both δ_{gb} and λ^*values listed in Table 1 are in agreement with previously reported ones in the literature. Fig. 7**(b)** displays a correlation between the potential barrier and space-charge layer width, which denotes an inverse dependence for such quantities. As a whole, the incorporation of doping cations in BCN-18 crystal structure tends to reduce the width of the space-charge layer. Fig. 7**(c)** exhibits the normalized protonic defect concentration estimated at 363 K in ambient condition for BCN-18 and BCN-Y ceramics. At the grain boundary core (r = 0) the normalized concentration value for BCN-Y is almost two orders of magnitude less than that for BCN-18, visually explaining the blocking phenomenon in doped samples.

Our results have a direct interpretation: the defect engineering employed to create oxygen vacancies for protonic defect formation via dissociative adsorption of water leads to an increase in the grain conductivity (σ_g), as predicted by the next defect model:

$$2O_O^x + R_2O_3 + 2Nb_{Nb}^x \rightarrow 2R_{Nb}^{||} + 2V_O^{\bullet\bullet} + Nb_2O_5, \quad (7)$$

where $R = Y^{3+}$, Gd^{3+}, Sm^{3+} or Nd^{3+}. Nevertheless, the grain boundary conductivity decreased after the incorporation of dopant cations in the crystal structure, resulting in the blocking process of charge carriers by the space-charge layer. For applications, the blocking effect should be reduced or avoided, as it contributes to a higher total electrical resistivity. Since grain boundary properties are also determined by geometrical properties, as described in the context of the brick-layer model, new configurations may be designed to prevent such blocking of the charge carriers at the grain boundary regions.

5. Conclusions

In summary, we have investigated the intrinsic origin of the blocking effect in a promising proton conductor for PC-SOFCs based on the ordered perovskite with chemical formula $Ba_3Ca_{1.18}Nb_{1.82-x}R_xO_{9-\delta}$, where *R* denotes the doping cations Y^{3+}, Gd^{3+}, Sm^{3+} and Nd^{3+} for $x = 0.30$. The 1:1 B-site ordering at long-range was verified in our ceramic samples by the presence of (111) reflections in all the X-ray diffraction patterns. Raman spectroscopy also confirmed the occurrence of the 1:1 order in all the BCN-*R* ceramics. No minor secondary phase appeared in the studied samples according with PXRD and EDXS analysis. Impedance spectroscopy technique combined with the brick-layer model was successfully applied to separate the contributions of the grains and grain boundaries to the electrical response of the proton conducting ceramics. We have found an increase in the grain conductivity in doped ceramics. Simultaneously the grain boundaries have

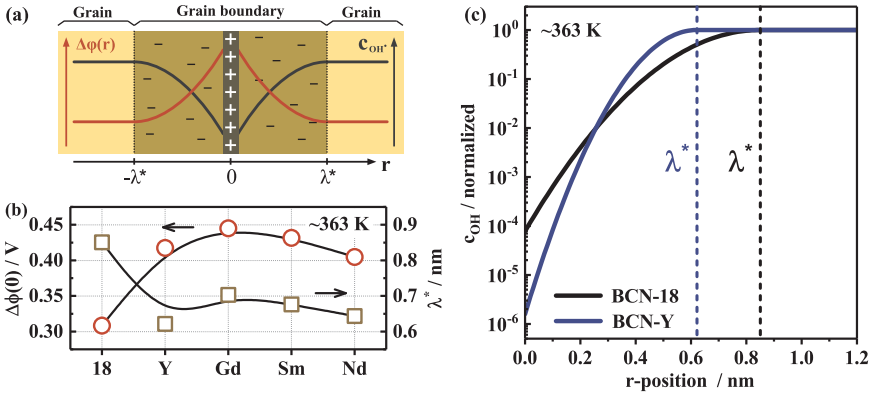

Fig. 7. (a) Space charge modeling of a grain boundary region with a positive core surrounded by negative space charge layers. Black and red curves are hydroxyl and electrical ones, respectively. Potential has a maximum value of φ(0) and grain boundary length extends from –λ* to +λ* with respect to a one-dimensional coordinate r centered at the core. (b) Δφ(0) and λ* calculated from impedance data for all the studied compositions at ~ 363 K. (c) Concentration profiles at space-charge region at ~ 363 K calculated for BCN-18 and BCN-Y data normalized with respect to bulk concentrations.

increased their blocking action of the charge carriers. In light of space-charge model, the Schottky barrier height was determined for all the compositions at different temperatures, showing that the doped ceramics have an increased barrier height in comparison with undoped ones. It means that the proton depletion in the space-charge layer may be responsible for the reduction of the grain boundary conductivity in doped compositions. Our result has an important contribution to the development of new proton conducting ceramics for PC-SOFCs in the sense that the space-charge properties should be taken into account for the understanding and then preventing of the blocking effect at the grain boundaries of materials optimized by atomic substitutions.

Acknowledgements

We are grateful for the Brazilian agencies CAPES, CNPq (proc. number 150936/2017-6), INCTMN (proc. number 2008/57872-1) and FAPESP (proc. number 2013/07296-2).

Appendix A. Supporting information

Supplementary data associated with this article can be found in the online version at http://dx.doi.org/10.1016/j.ceramint.2018.03.121.

References

[1] M.R. Karim, K. Hatakeyama, M. Koinuma, S. Hayami, Proton conductors produced by chemical modifications of carbon allotropes, perovskites and metal organic frameworks, J. Mater. Chem. A 5 (2017) 7243–7256.
[2] S. Hossain, A.M. Abdalla, S.N.B. Jamain, J.H. Zaini, A.K. Azad, A review on proton conducting electrolytes for clean energy and intermediate temperature-solid oxide fuel cells, Renew. Sustain. Energy Rev. 79 (2017) 750–764.
[3] N. Kochetova, I. Animitsa, D. Medvedev, A. Demin, P. Tsiakaras, Recent activity in the development of proton-conducting oxides for high-temperature applications, RSC Adv. 6 (2016) 73222–73268.
[4] E. Fabbri, D. Pergolesi, E. Traversa, Materials challenges toward proton-conducting oxide fuel cells: a critical review, Chem. Soc. Rev. 39 (2010) 4355–4369.
[5] D.R. Clark, H. Zhu, D.R. Diercks, S. Ricote, R.J. Kee, A. Almansoori, et al., Probing grain-boundary chemistry and electronic structure in proton-conducting oxides by atom probe tomography, Nano Lett. 16 (2016) 6924–6930.
[6] C.-T. Chen, C.E. Danel, S. Kim, On the origin of the blocking effect of grain-boundaries on proton transport in yttrium-doped barium zirconates, J. Mater. Chem. 21 (2011) 5435.
[7] L. Guan, S. Le, S. He, X. Zhu, T. Liu, K. Sun, Densification behavior and space charge blocking effect of Bi_2O_3 and Gd_2O_3 Co-doped CeO_2 as electrolyte for solid oxide fuel cells, Electrochim. Acta 161 (2015) 129–136.
[8] C. Kjølseth, H. Fjeld, Ø. Prytz, P.I. Dahl, C. Estournès, R. Haugsrud, et al., Space–charge theory applied to the grain boundary impedance of proton conducting $BaZr_{0.9}Y_{0.1}O_{3-\delta}$, Solid State Ion. 181 (2010) 268–275.
[9] D.A. Medvedev, J.G. Lyagaeva, E.V. Gorbova, A.K. Demin, P. Tsiakaras, Advanced materials for SOFC application: strategies for the development of highly conductive and stable solid oxide proton electrolytes, Prog. Mater. Sci. 75 (2016) 38–79.
[10] S. Wang, F. Zhao, L. Zhang, K. Brinkman, F. Chen, Doping effects on complex perovskite $Ba_3Ca_{1.18}Nb_{1.82}O_{9-\delta}$ intermediate temperature proton conductor, J. Power Sources 196 (2011) 7917–7923.
[11] S. Wang, L. Zhang, Z. Yang, L. Zhang, S. Fang, K. Brinkman, et al., Two-step co-sintering method to fabricate anode-supported $Ba_3Ca_{1.18}Nb_{1.82}O_{9-\delta}$ proton-conducting solid oxide fuel cells, J. Power Sources 215 (2012) 221–226.
[12] S. Wang, Y. Chen, S. Fang, L. Zhang, M. Tang, K. An, et al., Novel chemically stable $Ba_3Ca_{1.18}Nb_{1.82-x}Y_xO_{9-\delta}$ proton conductor: improved proton conductivity through tailored cation ordering, Chem. Mater. 26 (2014) 2021–2029.
[13] Z. Zhu, E. Guo, Z. Wei, H. Wang, Tailoring $Ba_3Ca_{1.18}Nb_{1.82}O_{9-\delta}$ with NiO as electrolyte for proton-conducting solid oxide fuel cells, J. Power Sources 373 (2018) 132–138.
[14] Y. Du, A.S. Nowick, Structural transitions and proton conduction in nonstoichiometric $A_3B'B''_2O_9$ Perovskite-type oxides, J. Am. Ceram. Soc. 78 (1995) 3033–3039.
[15] I.M. Hodge, M.D. Ingram, A.R. West, Impedance and modulus spectroscopy of polycrystalline solid electrolytes, J. Electroanal. Chem. Interfacial Electrochem. 74 (1976) 125–143.
[16] T. van Dijk, A.J. Burggraaf, Grain boundary effects on ionic conductivity in ceramic $Gd_xZr_{1-x}O_{2-(x/2)}$ solid solutions, Phys. Status Solidi 63 (1981) 229–240.
[17] M.A. Hernández, N. Masó, A.R. West, On the correct choice of equivalent circuit for fitting bulk impedance data of ionic/electronic conductors, Appl. Phys. Lett. 108 (2016).
[18] S.M. Haile, D.L. West, J. Campbell, The role of microstructure and processing on the proton conducting properties of gadolinium-doped barium cerate, J. Mater. Res. 13 (1998) 1576–1595.
[19] C. Kjølseth, H. Fjeld, Ø. Prytz, P.I. Dahl, C. Estournès, R. Haugsrud, et al., Space–charge theory applied to the grain boundary impedance of proton conducting $BaZr_{0.9}Y_{0.1}O_{3-\delta}$, Solid State Ion. 181 (2010) 268–275.
[20] M. Shirpour, B. Rahmati, W. Sigle, P.A. van Aken, R. Merkle, J. Maier, Dopant segregation and space charge effects in proton-conducting $BaZrO_3$ perovskites, J. Phys. Chem. C 116 (2012) 2453–2461.
[21] F. Iguchi, C.-T. Chen, H. Yugami, S. Kim, Direct evidence of potential barriers at grain boundaries in Y-doped $BaZrO_3$ from dc-bias dependence measurements, J. Mater. Chem. 21 (2011) 16517.
[22] M. Shirpour, R. Merkle, J. Maier, Space charge depletion in grain boundaries of $BaZrO_3$ proton conductors, Solid State Ion. 225 (2012) 304–307.
[23] D. Johnson, Software ZView 3.2, Scribner Associates, Inc, Southern Pines, 2009.
[24] J.E. Rodrigues, D.M. Bezerra, A.C. Hernandes, Ordering effect on the electrical properties of stoichiometric $Ba_3CaNb_2O_9$ based perovskite ceramics, Ceram. Int. 43 (2017) 14015–14022.
[25] O. Valdez-Ramírez, F. Gómez-García, M.A. Camacho-López, E. Ruiz-Trejo, Influence of the calcium excess in the structural and spectroscopic properties of the complex perovskite $Ba_3CaNb_2O_9$, J. Electroceram. 28 (2012) 226–232.
[26] R.L. Moreira, F.M. Matinaga, A. Dias, Raman-spectroscopic evaluation of the long-range order in $Ba(B'_{1/3}B''_{2/3})O_3$ ceramics, Appl. Phys. Lett. 78 (2001) 428.
[27] J.E.F.S. Rodrigues, E. Moreira, D.M. Bezerra, A.P. Maciel, C.W. de Araujo, Paschoal, Ordering and phonons in $Ba_3CaNb_2O_9$ complex perovskite, Mater. Res. Bull. 48 (2013) 3298–3303.
[28] P. Parayanthal, F.H. Pollak, Raman scattering in alloy semiconductors: "spatial correlation" model, Phys. Rev. Lett. 52 (1984) 1822–1825.
[29] E. Ruiz-Trejo, R.A. De Souza, Dopant substitution and oxygen migration in the complex perovskite oxide $Ba_3CaNb_2O_9$: a computational study, J. Solid State Chem. 178 (2005) 1959–1967.
[30] R. Gerhardt, A.S. Nowick, Grain-boundary effect in ceria doped with trivalent cations: i, electrical measurements, J. Am. Ceram. Soc. 69 (1986) 641–646.
[31] C. Foschini, D.P. Souza, P. Paulin Filho, J. Varela, AC impedance study of Ni, Fe, Cu, Mn doped ceria stabilized zirconia ceramics, J. Eur. Ceram. Soc. 21 (2001) 1143–1150.
[32] X. Guo, W. Sigle, J. Fleig, J. Maier, Role of space charge in the grain boundary blocking effect in doped zirconia, Solid State Ion. 154–155 (2002) 555–561.
[33] X. Guo, R. Waser, Electrical properties of the grain boundaries of oxygen ion conductors: acceptor-doped zirconia and ceria, Prog. Mater. Sci. 51 (2006) 151–210.